

## Research Article

# Luminescence Nanothermometry Based on $\text{Pr}^{3+} : \text{LaF}_3$ Single Core and $\text{Pr}^{3+} : \text{LaF}_3/\text{LaF}_3$ Core/Shell Nanoparticles

M. S. Pudovkin , D. A. Koryakovtseva, E. V. Lukinova, S. L. Korableva ,  
R. Sh. Khusnutdinova, A. G. Kiiamov , A. S. Nizamutdinov, and V. V. Semashko

Kazan Federal University, Institute of Physics, Kazan, Tatarstan 420008, Russia

Correspondence should be addressed to M. S. Pudovkin; jaz7778@list.ru

Received 12 April 2019; Accepted 17 June 2019; Published 4 September 2019

Academic Editor: Zhiping Luo

Copyright © 2019 M. S. Pudovkin et al. This is an open access article distributed under the Creative Commons Attribution License, which permits unrestricted use, distribution, and reproduction in any medium, provided the original work is properly cited.

Core  $\text{Pr}^{3+} : \text{LaF}_3$  ( $C_{\text{Pr}} = 1\%$ ) plate-like nanoparticles (nanoplates), core/shell  $\text{Pr}^{3+} : \text{LaF}_3$  ( $C_{\text{Pr}} = 1\%$ )/ $\text{LaF}_3$  nanoplates, core  $\text{Pr}^{3+} : \text{LaF}_3$  ( $C_{\text{Pr}} = 1\%$ ) sphere-like nanoparticles (nanospheres), and core/shell  $\text{Pr}^{3+} : \text{LaF}_3$  ( $C_{\text{Pr}} = 1\%$ )/ $\text{LaF}_3$  nanospheres were synthesized via the coprecipitation method of synthesis. The nanoparticles (NPs) were characterized by means of transmission electron microscopy, X-ray diffraction, and optical spectroscopy. The formation of the shell was proved by detecting the increase in physical sizes, sizes of coherent scattering regions, and luminescence lifetimes of core/shell NPs comparing with single core NPs. The average physical sizes of core nanoplates, core/shell nanoplates, core nanospheres, and core/shell nanospheres were  $62.2 \pm 0.9$ ,  $74.7 \pm 1.2$ ,  $13.8 \pm 0.9$  and  $22.0 \pm 1.2$  nm, respectively. The formation of the NP shell led to increasing of effective luminescence lifetime  $\tau_{\text{eff}}$  of the  $^3\text{P}_0$  state of  $\text{Pr}^{3+}$  ions for the core nanoplates, core/shell nanoplates, core nanospheres, and core/shell nanospheres the values of  $\tau_{\text{eff}}$  were 2.3, 3.6, 3.2, and  $4.7 \mu\text{sec}$ , respectively (at 300 K). The values of absolute sensitivity  $S_a$  for fluorescence intensity ratio (FIR) thermometry was  $0.01 \text{ K}^{-1}$  at 300 K for all the samples. The FIR sensitivity can be attributed to the fact that  $^3\text{P}_1$  and  $^3\text{P}_0$  states share their electronic populations according to the Boltzmann process. The values of  $S_a$  for lifetime thermometry for core nanoplates, core/shell nanoplates, core nanospheres, and core/shell nanospheres were  $(36.4 \pm 3.1) \cdot 10^{-4}$ ,  $(70.7 \pm 5.9) \cdot 10^{-4}$ ,  $(40.7 \pm 2.6) \cdot 10^{-4}$ , and  $(68.8 \pm 2.4) \cdot 10^{-4} \text{ K}^{-1}$ , respectively.

## 1. Introduction

Nanothermometry aims to measure the local temperature of a studied system with submicrometric spatial resolution [1, 2]. Among different methods of nanothermometry such as using nanoscale thermocouples [3] and coulomb blockade nanothermometers [4], the luminescent nanothermometers hold a special place because of its high spatial and temporal resolution, accuracy, and contactlessness [1, 4–7]. Rare-earth-doped nanomaterials hold a special role in luminescent nanothermometry among other luminescent nanomaterials because of their excellent photostability [8, 9], long luminescent lifetimes [10, 11], sharp emission bands, high brightness [12, 13], high melting point, promising magnetic properties [14, 15], and good resistance to thermal and chemical attacks [16, 17]. More importantly, rare earth ions doped into fluoride nanoparticles demonstrate even better optical properties in comparison with some counterparts

[18]. Nanofluorides are chosen as the host not only because of their low phonon energy but also because of their desirable chemical stability and low toxicity [19–21].

Indeed, over the past decade, interest in nanothermometry based on rare-earth-doped fluoride nanoparticles has increased significantly [22–25]. On the one hand, nanosized dimensionality of the luminescent nanothermometers allows them to come into contact with the studied small system providing accurate and precise temperature measurement [16]. The work in visible light provides high spatial resolution ( $\sim \lambda/2$ ). On the other hand, because of the high surface to volume ratio of nanosized objects the nanothermometer's luminescence can significantly be reduced by surficial defects and high vibronic molecules which increase nonradiative decay probability [19, 26]. These adverse effects can be avoided or at least can be reduced by the formation of core/shell structure which prevents direct contact of surface ions with quenchers.

Usually, the core serves as a scintillator, and the shell plays such screening “defensive” role although a set of functions of both core and shell can be more complicated [11, 26, 27]. In order to synthesize such core/shell NPs, the conventional coprecipitation [28] and hydrothermal methods [29] of synthesis have successfully been adopted during the last decade. The use of rare earth ions allows working into a broad range of wavelengths from ultraviolet ( $\text{Dy}^{3+}$  [30]) and visible light ( $\text{Er}^{3+}$  [7] and  $\text{Pr}^{3+}$  [22]) to near-infrared light ( $\text{Nd}^{3+}$  [31]) for industrial, biological, and medical applications.

Generally, there are six parameters that define the luminescence emission of material: intensity, lifetime, band shape, bandwidth, polarization, and spectral position [1]. Therefore, the luminescent nanothermometers can be grouped into six corresponding subclasses. The most widespread are the subclasses of luminescent nanothermometers based on the analysis of relative fluorescence intensity between the different emission bands corresponding to the suitable transitions and luminescent nanothermometers based on the analysis of luminescence lifetime. These methods cannot be affected by external conditions such as the fluctuation of the intensity of excitation light, the alteration of coupling degree, and the efficiency of optical fiber transmission electron microscopy (TEM). These facts make them very promising and highly developing.

In this case, the  $\text{Pr}^{3+}$  ion is very attractive for both methods. For the  $\text{Pr}^{3+}$  ions, the energy gap between  $^3\text{P}_0$  and the next-highest state,  $^3\text{P}_1$ , is only a few hundred  $\text{cm}^{-1}$  for most host matrices.  $^3\text{P}_1$  becomes thermally populated following  $^3\text{P}_0$  excitation, and the luminescence spectrum contains both  $^3\text{P}_0$  and  $^3\text{P}_1$  emissions, with intensity ratios consistent with the predicted Boltzmann distribution among these states [22, 32–34]. The work [26] demonstrates the applicability of  $5d \rightarrow 4f$  luminescence with the intra- $f^2$  transitions of  $\text{Pr}^{3+}$  covering a wide temperature range (10–1000 K). However, there are very few studies devoted to luminescence nanothermometry (especially lifetime thermometry) of rare-earth-doped nanoparticles of different morphology and structure including core/shell structure.

However, it should be noted that the lifetime thermometry is more complicated because of the complexity of lifetime curves and their interpretation for nanosized materials. Indeed, in bulk crystals, the lifetime curves of doping ions in the majority of cases can be described by exponential curves. However, the lifetime curves of doping ions in nanosized materials are more complicated. Indeed, in the nanoparticles, the role of the surface is increased, and the number of defects is higher. More importantly, the doping ions form clusters. These phenomena affect the crystal field around the doping ions which makes the shape of the lifetime curves more complicated in comparison with analogous bulk crystals [35, 36]. For these reasons, the modern theoretical approaches for some rare earth ions in some matrices are developed [36–38]. However, universal theories are still in the design phase. In order to estimate the luminescence lifetime values, the equation from [39] for an effective lifetime is used. Although this equation does not take into control the different abovementioned features of

nanomaterials, it still allows obtaining a numerical value of luminescence lifetime.

The main goal of the paper is the demonstration of the applicability of  $\text{Pr}^{3+}:\text{LaF}_3$  NPs in luminescence thermometry based on both spectral ratio and luminescent lifetime. We analyze the temperature-dependent luminescence features of  $\text{Pr}^{3+}:\text{LaF}_3$  ( $C_{\text{Pr}} = 1\%$ ) spherical-like NPs (nanospheres) and  $\text{Pr}^{3+}:\text{LaF}_3$  ( $C_{\text{Pr}} = 1\%$ ) plate-like NPs (nanoplates) as well as  $\text{Pr}^{3+}:\text{LaF}_3$  ( $C_{\text{Pr}} = 1\%$ )/ $\text{LaF}_3$  nanospheres and  $\text{Pr}^{3+}:\text{LaF}_3$  ( $C_{\text{Pr}} = 1\%$ )/ $\text{LaF}_3$  nanoplates covered with undoped  $\text{LaF}_3$  shell in 80–320 K temperature range. We characterize the NPs by means of TEM, X-ray diffraction (XRD), and optical spectroscopy. The formation of the shell for both nanospheres and nanoplates is proved by detecting the increase in the NP size and luminescent lifetimes after the shell formation. The NP size is determined via TEM. Additionally, the size of the coherent scattering region of all the NPs is determined via Debye–Scherrer and Williamson–Hall methods.

## 2. Materials and Methods

**2.1. Synthesis of the Nanoparticles.** The single core NPs were synthesized via the coprecipitation method [35]. In order to synthesize both  $\text{Pr}^{3+}:\text{LaF}_3$  ( $C_{\text{Pr}} = 1\%$ ) nanospheres and nanoplates, 0.04 g of  $\text{Pr}_2\text{O}_3$  and 4.00 g of  $\text{La}_2\text{O}_3$  were added to 85 mL of 10% nitric acid in a glass beaker. Both mixtures were heated to  $50^\circ\text{C}$  and stirred for 45 min until a transparent solution appeared. Then, the mixtures were filtered, poured into polypropylene glasses, and placed on magnetic mixers (400 revolutions per minute). The solutions of NaF were prepared by adding 3.8 g of NaF into 500 mL of deionized water. After filtration of the NaF solutions, the first one was swiftly poured for nanospheres and the second one was added dropwise for nanoplates. Then, the pH was adjusted to 4 by adding 25% solution of ammonium hydrate. Then both mixtures were stirring for 30 minutes (400 rpm), and finally, the NPs were washed by centrifugation (Janetski K24; 12000 rpm) using deionized water for several times.

In order to synthesize either  $\text{Pr}^{3+}:\text{LaF}_3$  ( $C_{\text{Pr}} = 1\%$ )/ $\text{LaF}_3$  core/shell nanospheres or nanoplates, 2.00 g of synthesized core NPs were suspended into 250 mL of deionized water at  $50^\circ\text{C}$ . The suspension was placed on magnetic mixers (400 rpm). The temperature of  $50^\circ\text{C}$  was maintained during the synthesis procedure. Then, the solution of 2.10 g/L of NaF was added into 100 mL of deionized water dropwise to the NPs suspension. Then, the mixture was stirred for 2 hours. After that, the solution of 7.00 g/L of  $\text{La}(\text{NO}_3)_3 \cdot 6\text{H}_2\text{O}$  was added into 150 mL of deionized water dropwise. Then, the mixture was stirred for 2 hours. Finally, it was washed by centrifugation (Janetski K24; 12000 rpm) using the deionized water for several times similarly to core NPs. All the samples were dried on air in dust-free box.

### 2.2. X-Ray Diffraction and Transmission Electron Microscopy.

The phase composition of the samples was characterized by an XRD method with the Shimadzu XRD-7000S X-ray diffractometer. Analysis of samples was carried out in a transmission electron microscope Hitachi HT7700 Exalens.

Sample preparation is as follows: 10 microliters of the suspension were placed on a formvar/carbon lacy 3 mm copper grid; drying was performed at room temperature. After drying, the grid was placed in a transmission electron microscope using a special holder for microanalysis. The analysis was held at an accelerating voltage of 100 kV in the TEM mode. The additional control of the amount of nitrates in a colloidal solution of the NPs after each stage of centrifugation was performed by the identification test using diphenylamine (the diphenylamine test).

**2.3. Optical Spectroscopy.** The luminescence spectra were recorded using the CCD spectrometer (StellarNet), which detects the emission in 200–1100 nm spectral range with a spectral resolution of 0.5 nm. The optical parametric oscillator laser system (420–1200 nm) from JV LOTIS TII was used for excitation of the luminescence of the samples. The pulse width and the pulse-repetition rate were 10 ns and 10 Hz, respectively. The spectral width of laser radiation was less than 0.15 nm. The experiments were carried out in 80–320 K temperature range. The luminescent lifetimes of  $\text{Pr}^{3+}$  ions were detected using BORDO 211A (10 bit and 200 MHz bandwidth) digital oscillograph and MDR-3 monochromator.

### 3. Results and Discussion

**3.1. Transmission Electron Microscopy.** In order to prove the formation of core/shell structured NPs, we demonstrate the increase in physical sizes, coherent scattering regions (CSR), and luminescent lifetimes of core/shell NPs comparing with single core ones. The increase in physical size and CSR of the NPs was estimated via TEM and XRD methods, respectively. The XRD data were analyzed using the well-known Debye–Scherrer [40] and Williamson–Hall [41] methods.

According to the TEM data (Figures 1 and 2), nanoplates and nanospheres differ between each other by size and shape. In order to build a size distribution for the nanoplates, the length of the nanoplates was measured.

According to Figures 1(a) and 1(b), both core and core/shell nanoplates form agglomerates consisting of the thin plates (~6 nm in thickness) on the formvar/carbon lacy copper grid. For both core and core/shell nanoplates, the interlayer distance between two fringes which are parallel to the upper and lower pedestals of the plate was measured to be ~0.35 nm which corresponds to the [002] plane of the  $\text{LaF}_3$  crystal. Hence, it can be suggested that the preferred growth of the nanoplates takes place along both [100] and [010] planes under the existing conditions of synthesis [42]. The average lengths of the core and core/shell nanoplates are  $62.2 \pm 0.9$  and  $74.7 \pm 1.2$  nm, respectively. The irregularity in the shape of the core/shell nanoplates seems to be less in comparison with the core ones.

On the one hand, both core and core/shell nanospheres are not perfectly spherical (Figures 2(a) and 2(b), respectively). Some of the nanospheres have an irregular shape. On the other hand, there is no preferential direction of growth unlike the nanoplates described above. For this

reason, we classified these NPs as spherical just for the sake of simplicity. The average diameters of the core and core/shell nanospheres are  $13.8 \pm 0.9$  and  $22.0 \pm 1.2$  nm, respectively, which proves the increase in the size of the particles after the shell formation.

**3.2. X-Ray Diffraction.** The XRD patterns of the core, core/shell nanoplates, and core, core/shell nanospheres are shown in Figures 3(a) and 3(b), respectively. According to the XRD data, all the NPs are hexagonal-structured nanocrystals that correspond to the structure of matrices of  $\text{LaF}_3$  and  $\text{PrF}_3$ . Sharp peaks and lack of peaks from impurities are observed, suggesting the high purity of these samples. For all the samples, the lattice parameters  $a$  and  $c$  were calculated. The lattice constants  $a$  and  $c$  are listed in Table 1. The lattice parameters for  $\text{LaF}_3$  (JCPDS–32–0483) are  $a = 0.7186$  and  $c = 0.7352$  nm. It is clearly seen that the lattice constants of the obtained samples are slightly bigger. Probably this difference can be explained by a larger number of defects, including water molecules in comparison with etalon bulk crystals. In turn, the lattice constants for both core and core/shell nanospheres are slightly larger than lattice constants of core and core/shell nanoplates. It can be related to the presence of captured water in nanospheres and/or other defects appearing due to the spontaneous character of the chemical reaction.

It is clearly seen from Figures 3(a) and 3(b) that the XRD peaks of the nanoplates are narrower than the XRD peaks of the nanospheres. Moreover, the nanospheres demonstrate a hint of an amorphous phase halo over the baseline unlike the nanoplates demonstrating lack of amorphous phase and consequently better crystallinity. Additionally, the signal-to-noise ratio for the nanoplates is higher than that for the nanospheres. It can be concluded that the slow dropwise addition of NaF solution provides better crystallinity comparing with a swift addition of NaF solution. Probably such relatively low crystallinity is a result of spontaneous character of the reaction in the coprecipitation method [42].

It is well known that nanoscale dimensionality of the crystalline particles leads to XRD peak broadening. Hence, the core/shell NPs should demonstrate narrower XRD peaks comparing with core ones. This phenomenon is clearly seen in Figures 3(c) and 3(d) showing normalized XRD patterns.

In order to additionally estimate the increase in the size of the NPs after the shell formation, the calculations of the size of the CSR via Debye–Scherrer and Williamson–Hall methods were carried out. It should be noted that the CSR is not a physical size of the NPs.

The following Debye–Scherrer formula is used [24]:

$$D = \frac{K\lambda}{\beta_D \cos \theta}, \quad (1)$$

where  $D$  is the size of the CSR,  $K$  is a shape factor (we used  $K = 0.9$ ),  $\lambda$  is the X-ray wavelength (0.15418 nm),  $\beta_D$  is the line broadening at half the maximum intensity (FWHM) in radians, and  $\theta$  is the Bragg angle in degrees. The distinguishable diffraction peaks having the lowest values of the signal-to-noise ratio are chosen. The CSR at different crystallographic

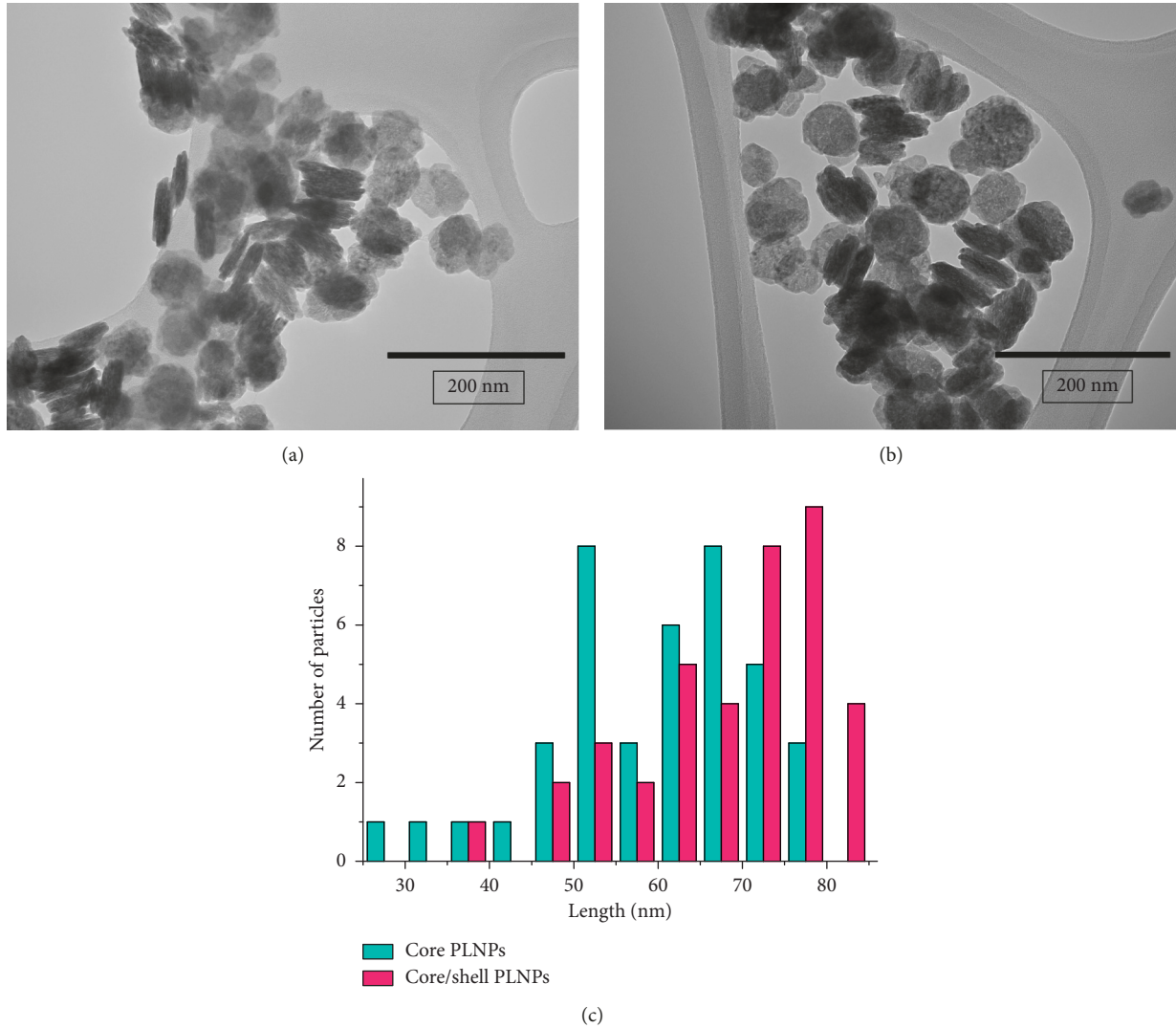


FIGURE 1: TEM image of (a) core nanoplates and (b) core/shell nanoplates. (c) The size distribution of core nanoplates and core/shell nanoplates.

orientations (hkl) for nanoplates and nanospheres are shown in Figures 4(a) and 4(b), respectively.

It is clearly seen in Figures 4(a) and 4(b) that the CSR of both nanoplates and nanospheres increases after the shell formation for all the chosen crystallographic orientations. For example,  $D_{002}$  for core and core/shell nanoplates are 13.6 and 16.7 nm, respectively.  $D_{002}$  for core and core/shell nanospheres are 9.1 and 12.0 nm, respectively. Moreover, the Debye–Scherrer calculations qualitatively prove the preferred direction of growth of the nanoplates along [100] and [010] planes. Indeed,  $D_{110}$  is 2 times higher than  $D_{002}$  for nanoplates (Figure 4(a)). Unlike  $D_{hkl}$  of the nanospheres does not demonstrate such a significant difference. This difference can be related to not perfectly spherical shape. The comparison of CSR of core nanoplates and core nanospheres for all the chosen crystallographic orientations is shown in Figure 4(c). It is additionally seen that the values of CSR of the nanoplates strongly depend on crystallographic orientations. In the case of nanospheres, such dependence is not

clear. It additionally confirms that the shape of the nanoplates is more irregular comparing with nanospheres.

Additionally, the XRD patterns were analyzed via the Williamson–Hall method [41]. This method allows obtaining values of CSR taking into control the contribution of strains to XRD peak broadening as follows:

$$\beta_{hkl} \cos \theta = \frac{K\lambda}{D} + 4\varepsilon \sin \theta, \quad (2)$$

where  $D$  is also the size of the CSR,  $K$  is the shape factor (we used  $K=0.9$ ),  $\lambda$  is the X-ray wavelength (0.15418 nm),  $\beta_{hkl}$  is the line broadening at half the maximum intensity (FWHM) in radians, and  $\theta$  is the Bragg angle in degrees. A plot (equation 2) is drawn with  $4 \sin \theta$  along the  $x$ -axis and  $\beta_{hkl} \cos \theta$  along the  $y$ -axis. From the linear fit to the data, the CSR was estimated from the  $y$  intercept, and the strain  $\varepsilon$  from the slope of the fit.

The Williamson–Hall plots for the nanoplates and nanospheres are shown on Figures 5(a) and 5(b), respectively.

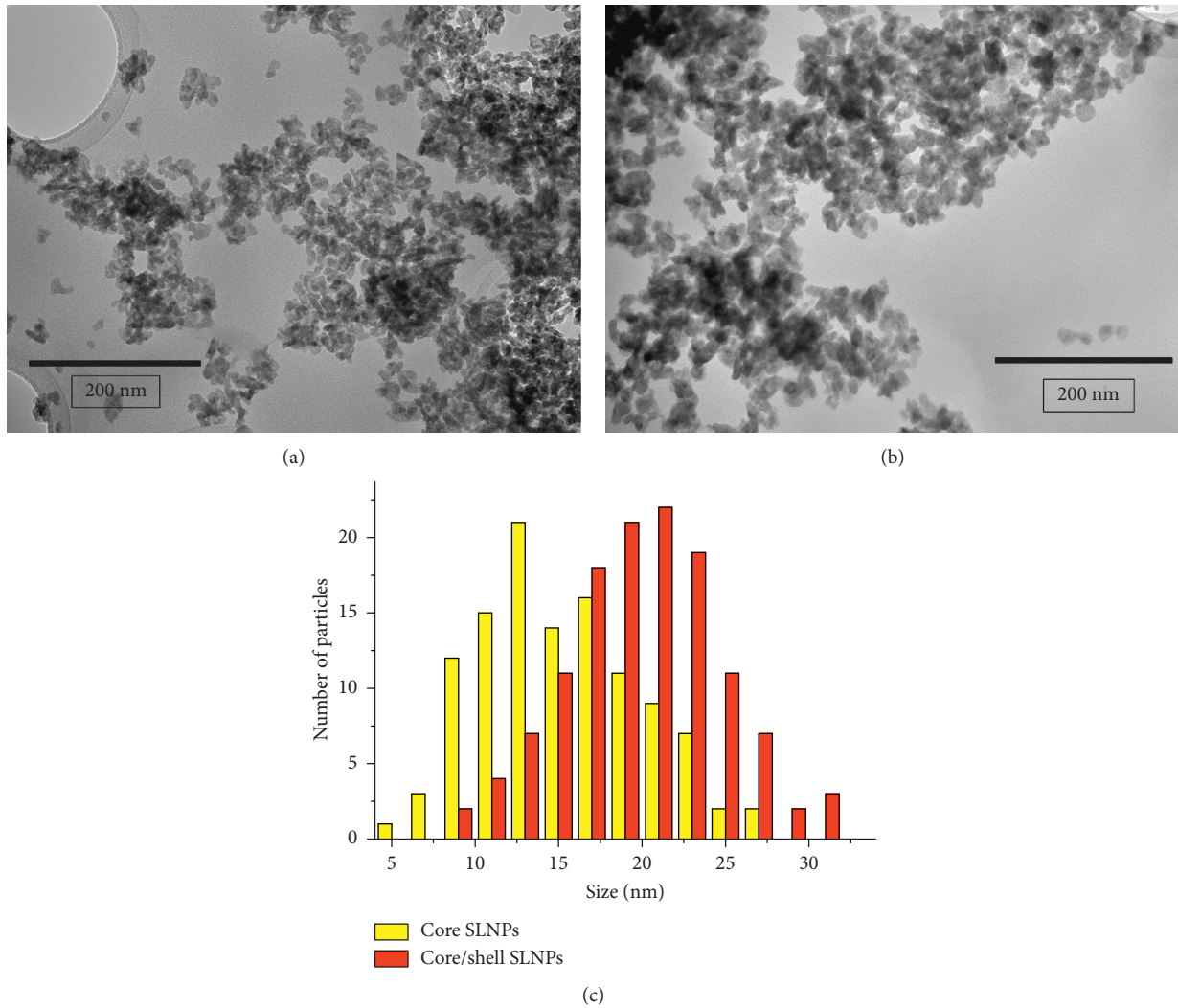


FIGURE 2: TEM image of (a) core nanospheres and (b) core/shell nanospheres. (c) The size distribution of core nanospheres and core/shell nanospheres.

For core and core/shell nanoplates, the values of the CSR are 23.1 and 37.4 nm, respectively. For core and core/shell nanospheres, the values of the CSR are 13.9 and 17.1 nm, respectively. According to both Debye–Scherrer and Williamson–Hall methods, the CSR of both core nanoplates and core increases with shell formation. Based on the conclusion that CSR is increased, it can be suggested that the shell grows around the core according to the core crystal structure instead of chaotic formation.

**3.3. Optical Spectroscopy.** Room-temperature luminescence spectra of both core nanoplates and core/shell nanoplates excited by a laser beam at 444 nm are presented in Figure 6(a). The luminescent spectra have the emission bands at about 487, 523, 537, 580, 601, and 672 nm which are interpreted as the result of the transition from  ${}^3P_j$  ( $j = 0, 1, 2$ ) excited states to  ${}^3H_4$ ,  ${}^3H_5$ ,  ${}^3H_6$ , and  ${}^3F_4$  states of  $\text{Pr}^{3+}$  ions, respectively [43]. The emission from the  ${}^1D_2$  state was not found under the excitation condition and in the studied temperature range. Probably the

emission from  ${}^1D_2$  is not observed because of the lack of nonradiative relaxation of  ${}^3P_j$  to  ${}^1D_2$  due to low cutoff phonon frequency in  $\text{LaF}_3$  ( $350\text{--}400\text{ cm}^{-1}$ ), which is 2 times less than one for YAG ( $700\text{--}865\text{ cm}^{-1}$ ). Indeed, to bridge the  ${}^3P_0\text{--}{}^1D_2$  energy gap, the 9 phonons are required in case of  $\text{LaF}_3$  and only 4 or 5 ones for YAG; thus, the multiphonon relaxation is expected to be negligible [44].

The lifetime curves of the samples are shown in Figures 6(b) and 6(c). All the lifetime curves are not single or double exponential. The shape of the lifetime curves is more complicated obviously due to a set of different physical processes taking place in the NPs. In [36], the complicated shape of lifetime curves of  $\text{Nd}^{3+}:\text{LaF}_3$  NPs synthesized via the coprecipitation method is explained by the presence of defects such as water molecules in the NPs core as well as on the NPs surface and by inhomogeneous distribution of doping ions. For these reasons, the effective luminescence lifetimes ( $\tau_{\text{eff}}$ ) were calculated using equation (3) [39] in order to compare the lifetimes of the samples:

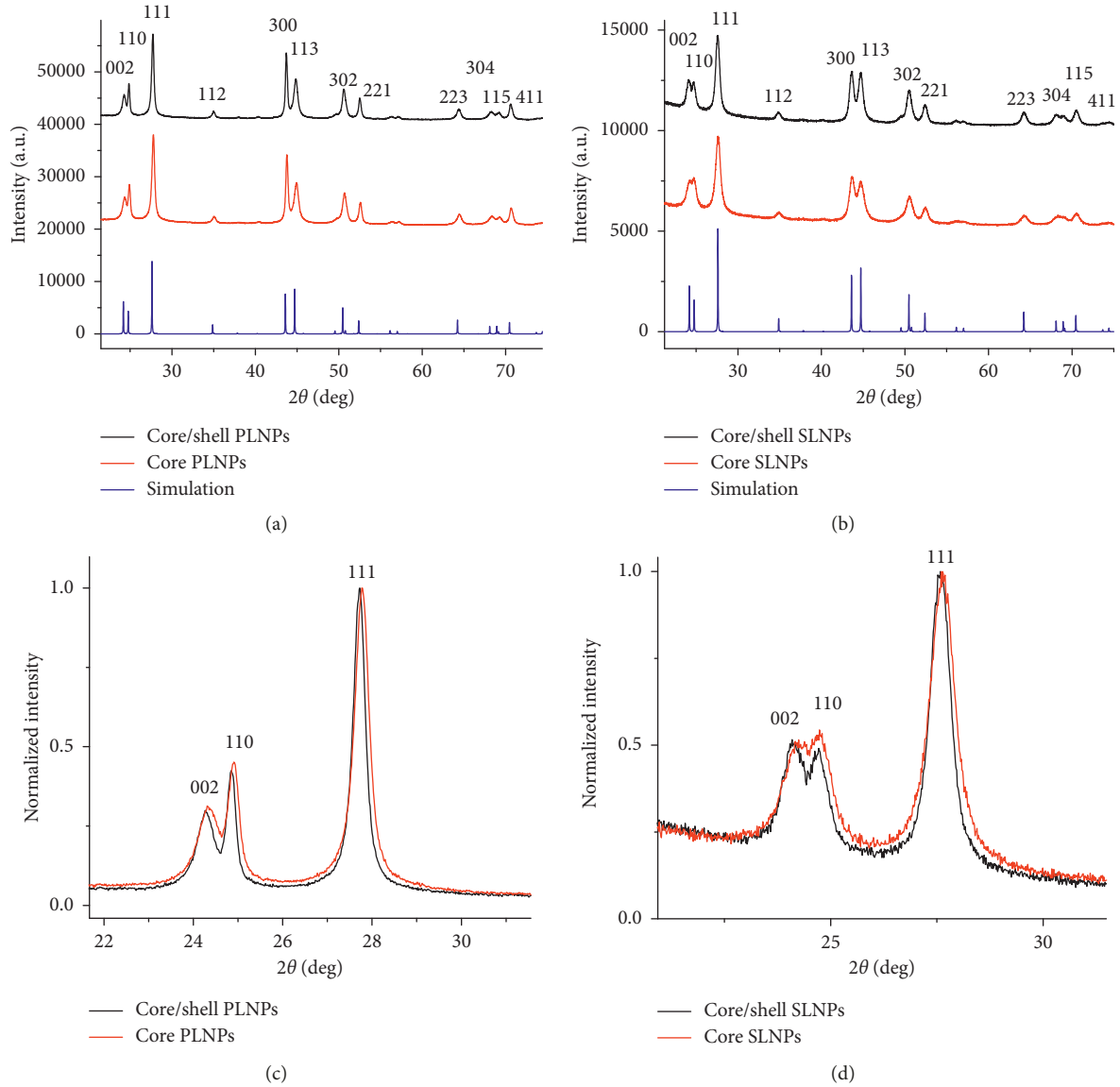


FIGURE 3: XRD patterns of the (a) core nanoplates and core/shell nanoplates and (b) core nanospheres and core/shell nanospheres. Normalized XRD patterns of the (c) core nanoplates and core/shell nanoplates and (d) core nanospheres and core/shell nanospheres.

TABLE 1: Lattice constants of the samples.

Lattice constant/sample	Core nanoplates	Core/shell nanoplates	Core nanospheres	Core/shell nanospheres
a (nm)	0.7316	0.7333	0.7494	0.7350
c (nm)	0.7476	0.7497	0.7512	0.7548

$$\tau_{\text{eff}} = \frac{\int_0^{\infty} tI(t)dt}{\int_0^{\infty} I(t)dt} \quad (3)$$

For the core nanoplates, core/shell nanoplates, core nanospheres, and core/shell nanospheres, the values of  $\tau_{\text{eff}}$  are 2.3, 3.6, 3.2, and 4.7  $\mu\text{sec}$ , respectively (at 300 K). It is clearly seen that the luminescence lifetime increases after shell formation for both nanoplates and nanospheres. It can be suggested that the shell reduces the amount of surface

defects as well as prevents the surface  $\text{Pr}^{3+}$  ions from contacting with surface quenchers. It should be noted that the values of  $\tau_{\text{eff}}$  are less than the lifetime for  $\text{Pr}^{3+}:\text{LaF}_3$  ( $C_{\text{Pr}} = 1\%$ ) crystal which additionally confirms the presence of quenchers.

**3.4. Intensity Ratio Thermometry.** Figure 7 exhibits the emission spectra of the core nanospheres as a function of temperature in 80–320 K range. The luminescence spectra of all the compounds do not present any change in the

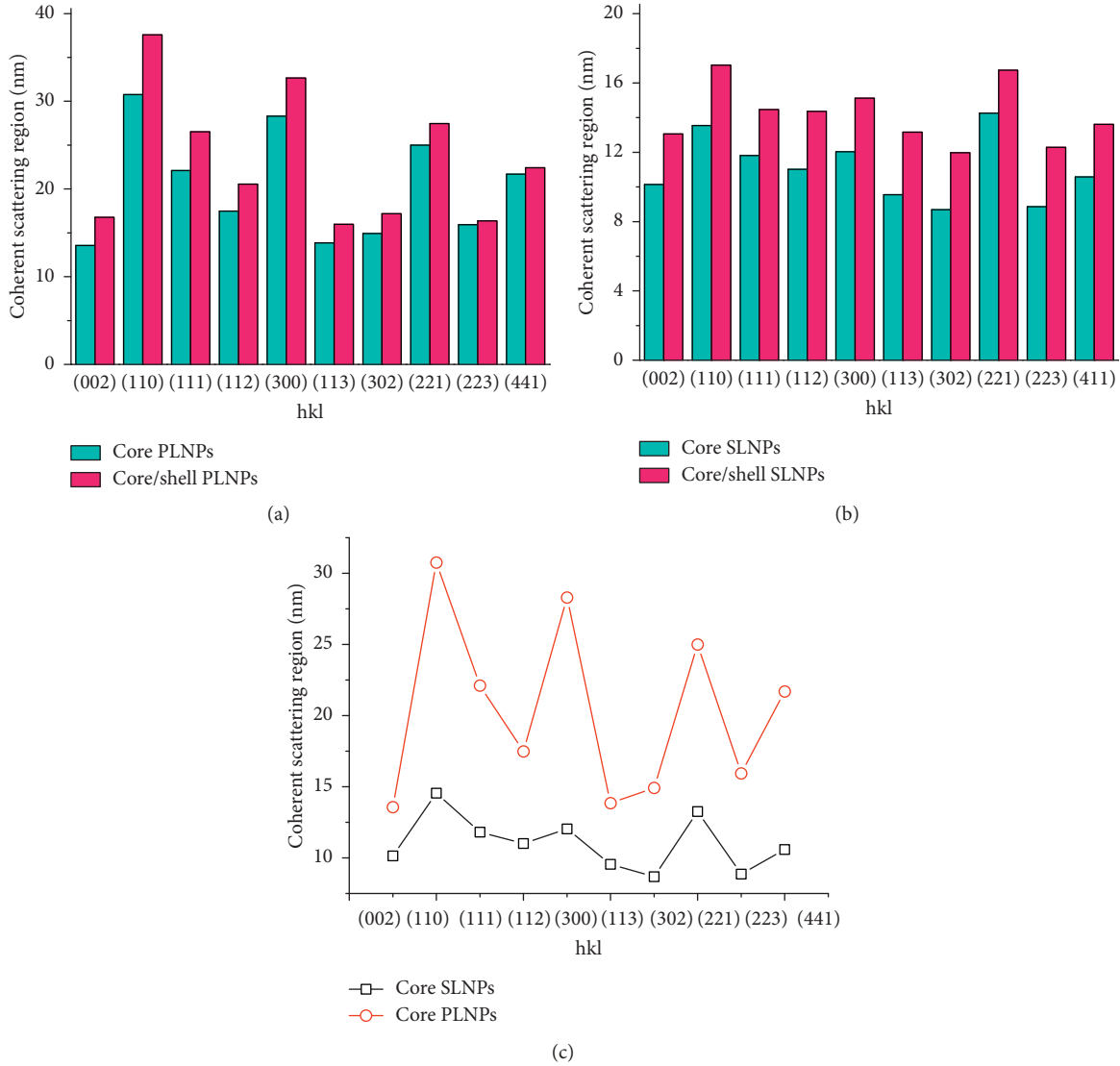


FIGURE 4: The Debye–Sherrer calculation of the coherent scattering regions of the (a) core nanoplates and core/shell nanoplates and (b) core nanospheres and core/shell nanospheres at different crystallographic orientations. (c) The comparison of the values of the coherent scattering regions of the core nanospheres and core nanoplates at different crystallographic orientations.

peak positions with the temperature increase. Herewith, the intensity of  ${}^3P_0$  emission decreases as the intensity of  ${}^3P_1$  increases in the whole 80–320 K temperature range. In the experimental set up, the NPs were excited by 444 pulse laser irradiation which corresponds to excitation from the  ${}^3H_4$  ground state to the  ${}^3P_2$  excited state. In our case after excitation of the  ${}^3P_2$  state, the  ${}^3P_2$ – ${}^3P_0$  non-radiative relaxation takes place. Then, the decrease in the intensity of the emission from  ${}^3P_0$  (at 487 nm or 537 nm) and simultaneous increase in the intensity of the emission from  ${}^3P_1$  (at 523 nm) can be attributed to the fact that  ${}^3P_1$  and  ${}^3P_0$  states share their electronic populations according to the Boltzmann process [22]. Thermalization of the  ${}^3P_1$  state begins at around 80 K and operates more and more efficiently upon warming. A fluorescence intensity ratio (FIR) arising from the  ${}^3P_1$  state to that arising from the  ${}^3P_0$  state can be described as [22]

$$R = B \exp\left(\frac{\Delta E}{k_B T}\right), \quad (4)$$

where  $B$  is a constant,  $\Delta E$  is the effective energy difference between the  ${}^3P_1$  and  ${}^3P_0$  states,  $k_B$  is the Boltzmann constant, and  $T$  is the absolute temperature. Two distinct emission bands at 523 and 532 nm, corresponding to the  ${}^3P_1 \rightarrow {}^3H_5$  and  ${}^3P_0 \rightarrow {}^3H_5$  transitions, respectively, were chosen for intensity ratio calculations. The FIR plots for all the samples are shown in Figure 8. As expected, the FIR for all the samples does not differ between each other and can be fitted by using the following formula:

$$R = 16.8 \exp\left(\frac{554}{k_B T}\right). \quad (5)$$

$\Delta E = 554 \pm 9 \text{ cm}^{-1}$  is in good agreement with the literature data [45].

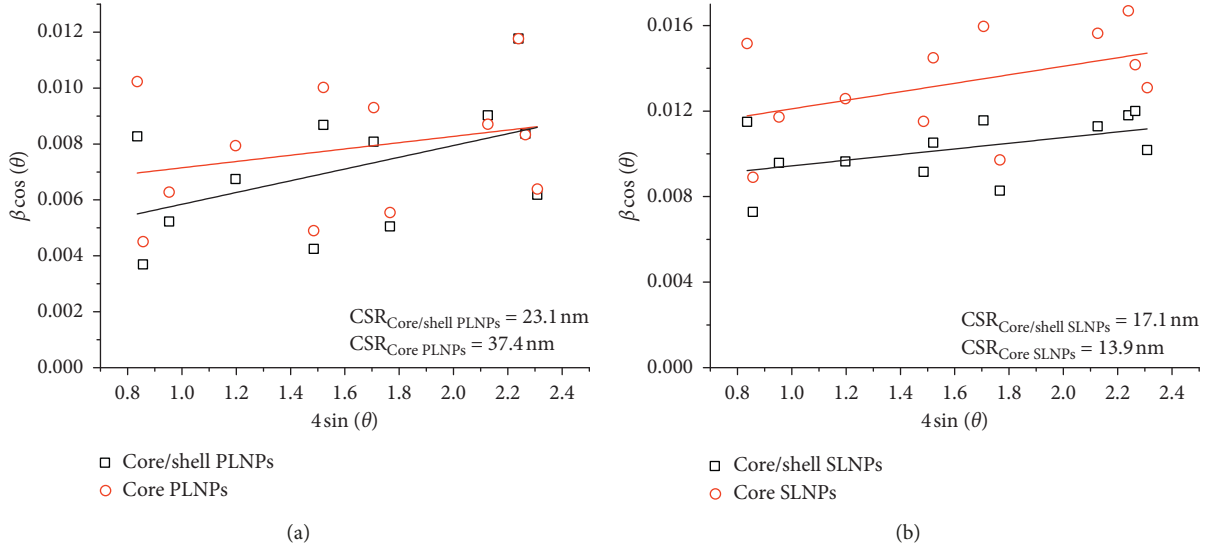


FIGURE 5: The Williamson-Hall plot of the (a) core nanoplates and core/shell nanoplates and (b) core nanospheres and core/shell nanospheres.

For temperature sensing applications, the absolute temperature sensitivity  $S_a$  and the relative temperature sensitivity  $S_r$  are the two very important parameters, corresponding to the absolute change and the relative change of the ratio  $R$  with respect to temperature variation, respectively. According to equation 1,  $S_a$  and  $S_r$  can be written as [22]

$$S_a = \frac{1}{R} \frac{dR}{dT} = \frac{\Delta E}{k_B T^2}, \quad (6)$$

$$S_r = \frac{dR}{dT} = R \left( \frac{\Delta E}{k_B T^2} \right).$$

$S_a$  plot of the samples is shown in Figure 9. For all the samples,  $S_a = 0.01 \text{ K}^{-1}$  at 300 K. As it is proved,  $S_a$  does not depend on the structure of the NPs. Even the core/shell nanospheres having the highest lifetime demonstrate the same intensity ratio temperature sensing. Hence, we studied the lifetime thermometry. The result is also superior to the  $S_a$  value of  $0.0034 \text{ K}^{-1}$  for the  $\text{Y}_2\text{O}_3:\text{Ti}^{3+}/\text{Yb}^{3+}$  sample [46] and that of  $0.0075 \text{ K}^{-1}$  for the  $\text{LiNbO}_3:\text{Er}^{3+}/\text{Yb}^{3+}$  sample [47] at 310 K.

**3.5. Luminescence Lifetime Thermometry.** Luminescence decay curves of the  $^3\text{P}_0$  state of  $\text{Pr}^{3+}$  ions for core nanoplates, core/shell nanoplates, core nanospheres, and core/shell nanospheres recorded at different temperatures upon 444 nm pulse laser excitation are shown in Figures 10(a)–10(d), respectively. All the curves keep their sophisticated shape in the whole temperature range. In order to estimate the influence of different processes on luminescence lifetime, the experimental lifetime  $t_{\text{exp}}$  can be defined as a sum of different terms that contribute into it [48]:

$$\frac{1}{\tau_{\text{exp}}} = \frac{1}{\tau_{\text{rad}}} + \frac{1}{\tau_{\text{NR}}} + \frac{1}{\tau_{\text{Q}}}, \quad (7)$$

where  $\tau_{\text{rad}}$  is the radiative contribution,  $\tau_{\text{NR}}$  is the non-radiative or multiphonon contribution, and  $\tau_{\text{Q}}$  is a term linked to the contribution of other quenching mechanisms, such as energy transfer to other lanthanide ions or additional quenchers.  $\tau_{\text{rad}}$  expressing the radiative transition rate has almost no temperature dependence [42, 48].  $\tau_{\text{NR}}$  expressing the nonradiative or multiphonon rate behaves in the opposite way. As it was mentioned above, the  $^1\text{D}_2$  emission was not found or seems to be negligible for  $\text{Pr}^{3+}:\text{LaF}_3$ . Hence, the lifetime of the  $^3\text{P}_0$  state is not influenced by multiphonon relaxation from  $^3\text{P}_0$  to  $^1\text{D}_2$  although this process is temperature dependent [49, 50]. As was discussed above, the rapid thermalization of the  $^3\text{P}_1$  level by  $^3\text{P}_0$  upon warming contributes to the temperature dependence of luminescence lifetime of the  $^3\text{P}_0$  state [51]. In particular, in [51], the temperature dependence of  $^3\text{P}_0$  state luminescence lifetime of  $\text{Pr}^{3+}$  in  $\text{Pr}^{3+}:\text{LaF}_3$  ( $C_{\text{Pr}} = 0.01\text{--}0.03\%$ ) is explained by this rapid thermalization of  $^3\text{P}_1$  only. Therefore,  $^3\text{P}_1$  and  $^3\text{P}_0$  states share their electronic populations according to the Boltzmann process and thermalization of the  $^3\text{P}_1$  state takes place. Hence, the Boltzmann process has significant contribution to the temperature dependence of luminescence lifetime of the  $^3\text{P}_0$  state. However, there are probably more temperature-dependent processes.

Indeed, the lifetime curves of the samples demonstrate a complicated shape (Figures 6(a) and 6(b)). It can be suggested that there are several physical processes which can be responsible for luminescence quenching [11]. Some of these processes can be temperature dependent. Hence, the  $\tau_{\text{Q}}$  term seems to have a contribution into the temperature dependence of luminescence lifetime [41]. However, due to different morphology and structure of the samples, the real contribution of the  $\tau_{\text{Q}}$  term to temperature sensitivity of  $^3\text{P}_0$  state luminescence lifetime can be different. In particular, for system  $\text{Pr}^{3+}:\text{LaF}_3$ , concentration quenching at high  $\text{Pr}^{3+}$  concentration takes place. It happens via cross-relaxation [52]. The energy migration between  $\text{Pr}^{3+}$  ions and final

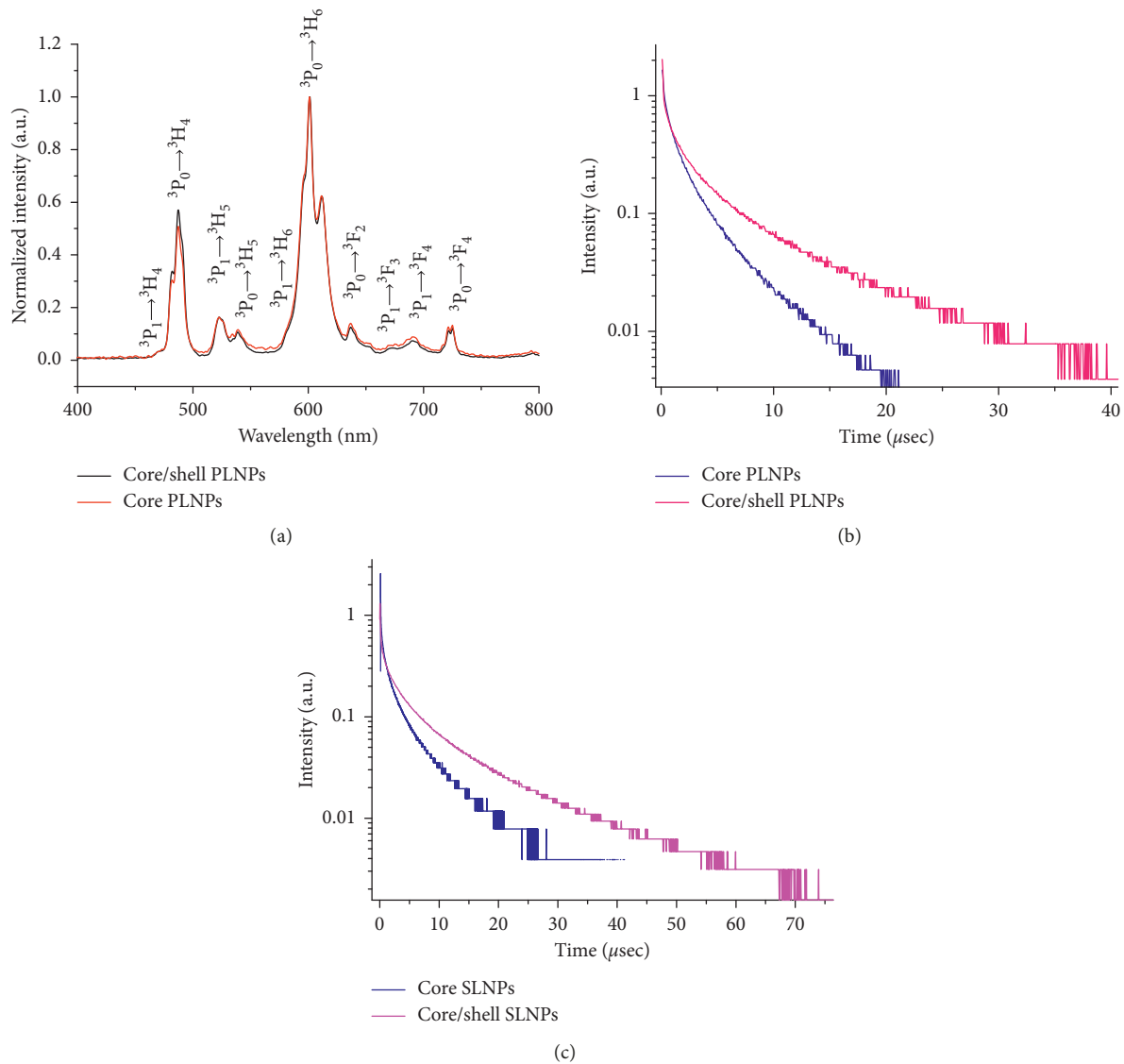


FIGURE 6: (a) Normalized at maximum (601 nm) room-temperature luminescence spectra of both core nanoplates and core/shell nanoplates ( $\lambda_{\text{ex}} = 444$  nm). (b) The luminescence lifetime curves of the  $^3P_0$  state of  $\text{Pr}^{3+}$  for core nanoplates and core/shell nanoplates at 300 K ( $\lambda_{\text{ex}} = 444$  nm,  $\lambda_{\text{em}} = 486$  nm). (c) The luminescence lifetime curves of the  $^3P_0$  state of  $\text{Pr}^{3+}$  for core nanospheres and core/shell nanospheres at 300 K ( $\lambda_{\text{ex}} = 444$  nm,  $\lambda_{\text{em}} = 486$  nm).

quenching by a defect is also possible. This quenching can be temperature dependent [52]. Indeed, at 1% concentration of  $\text{Pr}^{3+}$  ions, the quenching processes may take place. On the one hand, at the concentration of 0.01%, it is considered that the  $\text{Pr}^{3+}$  ions do not interact with each other in crystals. On the other hand, concentration such as 12% is very convenient for observing the cross-relaxation processes of  $\text{Pr}^{3+}$  ions. However, as it was mentioned above, in the NPs synthesized via the coprecipitation method, the inhomogeneity in concentrations of doping ions may take place. It means that the local concentration of the doping ions can be more than 1%. Doping ions form clusters where interaction between doping ions and subsequent luminescence quenching is more effective. Thus, it can be suggested that this inhomogeneity of  $\text{Pr}^{3+}$  distribution can lead to energy migration process which is temperature dependent

[52, 53]. The nature of defects in the samples is not well known. The samples can differ from each other by the nature of defects and their concentrations. Finally, it can be concluded that there are several temperature-dependent processes including thermalization of  $^3P_1$ , as well as temperature-dependent luminescence quenching processes.

As it was mentioned above, the shape of the lifetime curves is not single exponential or double exponential. The shape is complicated and it cannot be easily described. Hence, in order to estimate the lifetimes, equation 3 was used.  $\tau_{\text{eff}}$  temperature dependence plot should reflect the contributions of these processes without the specificity of each process. Figure 11 represents the temperature evolution of  $\tau_{\text{eff}}$  for all the samples. Surprisingly,  $\tau_{\text{eff}}$  temperature dependence can be fitted linearly. It is noteworthy that, in the case of linear fitting, the Pearson coefficient for all the

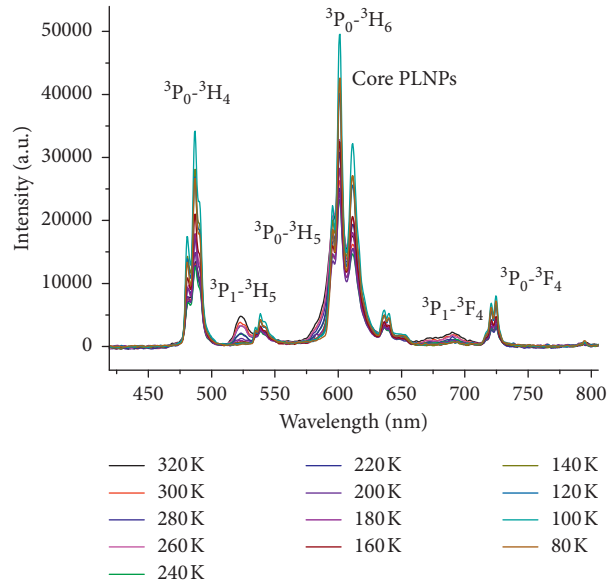


FIGURE 7: Luminescence spectra of the core nanospheres  $\text{Pr}^{3+}:\text{LaF}_3$  as a function of temperature obtained under laser excitation at  $444 \text{ nm} \pm$ .

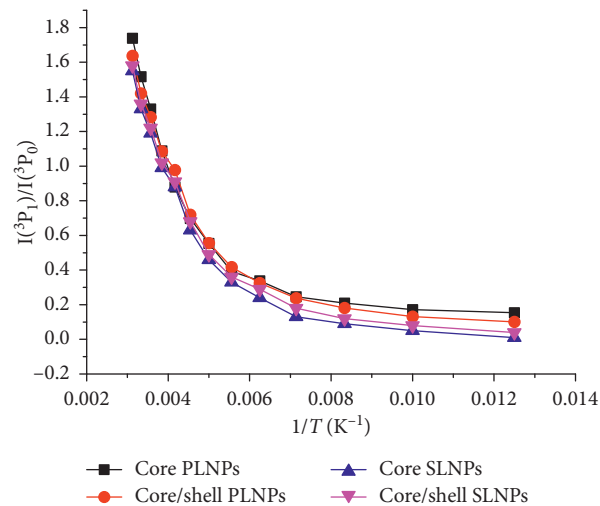


FIGURE 8: Luminescence intensity ratio of  ${}^3\text{P}_1\text{-}{}^3\text{H}_5$  and  ${}^3\text{P}_0\text{-}{}^3\text{H}_5$  emissions of  $\text{Pr}^{3+}$  ions for all the samples.

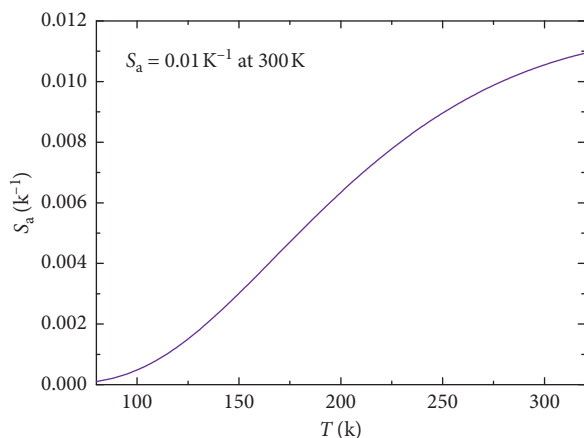


FIGURE 9: Temperature dependence of the absolute sensitivity  $S_a$  for all the samples.

samples is more than 0.9 which corresponds to good linearity of the results. Although the Boltzmann process is nonlinear in the whole studied temperature range, it seems that other sophisticated temperature-dependent quenching processes compensate nonlinearity of the Boltzmann process. It can be suggested that synergetic action of all abovementioned processes leads to simple linearity of  $\tau_{\text{eff}}$  temperature dependence. Both core nanoplates and nanospheres demonstrate almost the same values of temperature sensitivity ( $\sim 40 \cdot 10^{-4}$ ) which can be defined as the slope. In turn, both core-shell nanoplates and nanospheres demonstrate the same values of temperature sensitivity ( $\sim 70 \cdot 10^{-4}$ ) which are bigger than these values for core NPs. These differences in values of temperature sensitivities  $S_a$  are the subjects of further research. However, it can be suggested that the shell turns off some temperature-independent

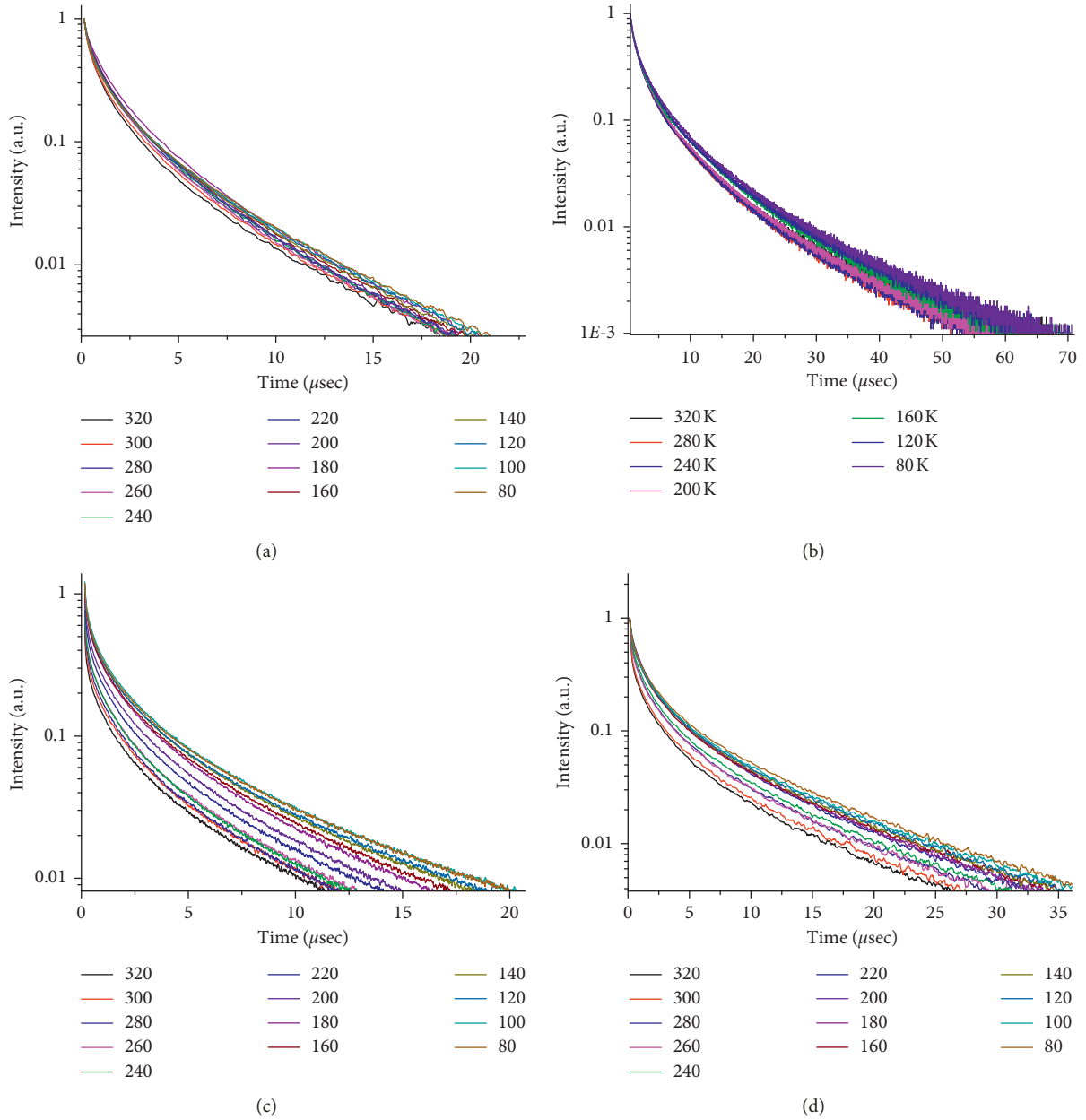


FIGURE 10: Fluorescence decay curves of  ${}^3P_0$  level recorded at different temperatures upon 444 nm laser excitation of core nanoplates (a), core/shell nanoplates (b), core nanospheres (c), and core/shell nanospheres (d).

quenching process which leads to increasing of temperature sensitivity based on luminescence lifetime.

Nevertheless,  $S_a$  based on FIR technique is notably higher  $\sim 100 \cdot 10^{-4} \text{ K}^{-1}$  in comparison with  $S_a$  based on luminescence lifetime. It seems that FIR thermometry is easier and more effective than lifetime thermometry.

**3.6. Temperature Uncertainty and Repeatability.** The thermometer performance is characterized not only by the relative sensitivity but also the maximum temperature uncertainty. The minimum temperature uncertainty can be estimated using

$$\delta T = \frac{1}{S_r} \frac{\delta D}{D}, \quad (8)$$

where  $\delta D/D$  is the relative uncertainty in the determination of the thermometric parameter (we use the typical  $\delta D/D$  value of a portable detector, 0.5%) [52]. The temperature uncertainty at 300 K for all the  $\text{Pr}^{3+}:\text{LaF}_3$  samples in FIR thermometry was  $0.5^\circ\text{C}$ . The repeatability of the thermometers readout upon temperature cycling is quantified using the following expression [48]:

$$R = 1 - \frac{\max(|\Delta_c - \Delta_i|)}{\Delta_c}, \quad (9)$$

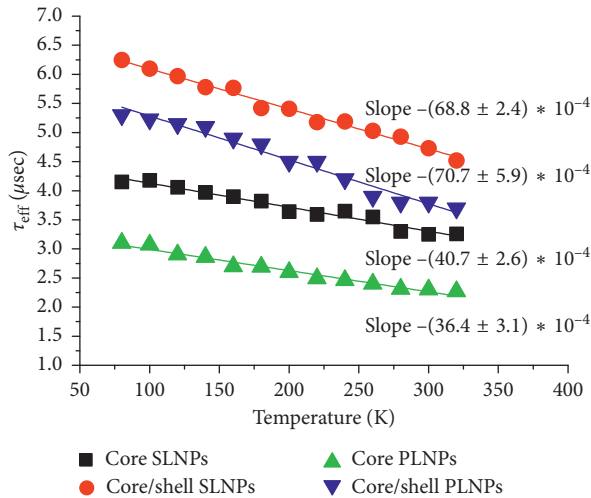


FIGURE 11: The values of  $\tau_{\text{eff}}$  of the samples at different temperatures.

where  $\Delta_c$  is the mean thermometric parameter (extracted from the calibration curve) and  $\Delta_i$  is the value of each measurement of the thermometric parameter. Usually, 10 consecutive measurements are enough to have a minimal statistical significance of the computed results. The thermometric parameter recorded in 10 heating-cooling temperature cycles showing reproducibility was around 99.1% for all the samples.

#### 4. Conclusions

The core  $\text{Pr}^{3+}:\text{LaF}_3$  ( $C_{\text{Pr}}=1\%$ ) plate-like nanoparticles (nanoplates), core/shell  $\text{Pr}^{3+}:\text{LaF}_3$  ( $C_{\text{Pr}}=1\%$ )/ $\text{LaF}_3$  nanoplates, core  $\text{Pr}^{3+}:\text{LaF}_3$  ( $C_{\text{Pr}}=1\%$ ) sphere-like nanoparticles (nanospheres), and core/shell  $\text{Pr}^{3+}:\text{LaF}_3$  ( $C_{\text{Pr}}=1\%$ )/ $\text{LaF}_3$  nanospheres were synthesized via the coprecipitation method of synthesis. The nanoparticles (NPs) were characterized by means of TEM, XRD, and optical spectroscopy. The formation of the shell was proved by detecting the increase in physical sizes, sizes of coherent scattering region, and luminescence lifetimes of core/shell NPs comparing with single core NPs. The average diameters of core nanoplates, core/shell nanoplates, core nanospheres, and core/shell nanospheres were  $62.2 \pm 0.9$ ,  $74.7 \pm 1.2$ ,  $13.8 \pm 0.9$ , and  $22.0 \pm 1.2$  nm, respectively. The formation of the NP shell led to increasing of effective luminescence lifetime  $\tau_{\text{eff}}$  of the  $^3\text{P}_0$  state of  $\text{Pr}^{3+}$  ions. For the core nanoplates, core/shell nanoplates, core nanospheres, and core/shell nanospheres, the values of  $\tau_{\text{eff}}$  were 2.3, 3.6, 3.2, and 4.7  $\mu\text{sec}$ , respectively (at 300 K). The values of absolute sensitivity  $S_a$  for fluorescence intensity ratio (FIR) thermometry was  $0.01 \text{ K}^{-1}$  at 300 K for all the samples. The FIR sensitivity can be attributed to the fact that  $^3\text{P}_1$  and  $^3\text{P}_0$  states share their electronic populations according to the Boltzmann process. The values of  $S_a$  for lifetime thermometry for core nanoplates, core/shell nanoplates, core nanospheres, and core/shell nanospheres were  $(36.4 \pm 3.1) \cdot 10^{-4}$ ,  $(70.7 \pm 5.9) \cdot 10^{-4}$ ,  $(40.7 \pm 2.6) \cdot 10^{-4}$ , and  $(68.8 \pm 2.4) \cdot 10^{-4} \text{ K}^{-1}$ , respectively. The difference in values of  $S_a$

for lifetime thermometry is attributed to the presence of several temperature-dependent luminescence quenching processes [44, 53, 54]. Since the samples differ between each other by morphology and structure, the contribution of these quenching processes (by different defects probably) is different. This phenomenon is the subject of further research. Finally,  $\text{Pr}^{3+}:\text{LaF}_3$  is well proven as an excellent material in different areas [53–55].

#### Data Availability

The TEM microscopy, XRD, spectra, and lifetime data used to support the findings of this study have been deposited in the Google disk repository (<https://drive.google.com/drive/folders/1V-2yCykljqfpech3ysKHcXthajYvkWg1?usp=sharing>). The size distribution, Debye–Scherrer, Williamson–Hall, and elemental analysis data used to support the findings of this study are included within the article. These data are available from the corresponding author upon request.

#### Conflicts of Interest

The authors declare that they have no conflicts of interest.

#### Acknowledgments

The chemical synthesis and material characterization works were supported by the subsidy allocated to Kazan Federal University for the state assignment in the sphere of scientific activities (3.1156.2017/4.6 and 3.5835.2017/6.7). The optical spectroscopy works were supported by the research grant of Kazan Federal University. Microscopy studies were carried out at the Interdisciplinary Center of Analytical Microscopy of Kazan Federal University.

#### References

- [1] D. Jaque and F. Vetrone, “Luminescence nanothermometry,” *Nanoscale*, vol. 4, no. 15, pp. 4301–4326, 2012.
- [2] V. Lojpur, G. Nikolić, and M. D. Dramićanin, “Luminescence thermometry below room temperature via up-conversion emission of  $\text{Y}_2\text{O}_3:\text{Yb}^{3+}, \text{Er}^{3+}$  nanophosphors,” *Journal of Applied Physics*, vol. 115, no. 20, pp. 203–106, 2014.
- [3] G. P. Szakmany, A. O. Orlov, G. H. Bernstein, and W. Porod, “Single-metal nanoscale thermocouples,” *IEEE Transactions on Nanotechnology*, vol. 13, no. 6, pp. 1234–1239, 2014.
- [4] J. P. Kauppinen and J. P. Pekola, “Coulomb blockade nanothermometer,” *Microelectronic Engineering*, vol. 41–42, pp. 503–506, 1998.
- [5] C. D. S. Brites, P. P. Lima, N. J. O. Silva et al., “Thermometry at the nanoscale,” *Nanoscale*, vol. 4, no. 16, pp. 4799–4829, 2012.
- [6] X.-d. Wang, O. S. Wolfbeis, and R. J. Meier, “Luminescent probes and sensors for temperature,” *Chemical Society Reviews*, vol. 42, no. 19, pp. 7834–7869, 2013.
- [7] M. L. Debasu, D. Ananias, I. Pastoriza-Santos, L. M. Liz-Marzán, J. Rocha, and L. D. Carlos, “All-in-one optical heater-thermometer nanoplatform operative from 300 to 2000 K based on  $\text{Er}^{3+}$  Emission and blackbody radiation,” *Advanced Materials*, vol. 25, no. 35, pp. 4868–4874, 2013.
- [8] D. Bekah, D. Cooper, K. Kudinov et al., “Synthesis and characterization of biologically stable, doped  $\text{LaF}_3$  nanoparticles co-conjugated to PEG and photosensitizers,” *Journal*

- of *Photochemistry and Photobiology A: Chemistry*, vol. 329, pp. 26–34, 2016.
- [9] Z. Xiaoting, T. Hayakawa, Y. Ishikawa, Y. Liushuan, and M. Nogami, “Structural investigation and  $\text{Eu}^{3+}$  luminescence properties of  $\text{LaF}_3:\text{Eu}^{3+}$  nanophosphors,” *Journal of Alloys and Compounds*, vol. 644, pp. 77–81, 2015.
  - [10] E. C. Ximendes, U. Rocha, K. U. Kumar, C. Jacinto, and D. Jaque, “ $\text{LaF}_3$  core/shell nanoparticles for subcutaneous heating and thermal sensing in the second biological-window,” *Applied Physics Letters*, vol. 108, no. 25, 2016.
  - [11] Y. Gu, Q. Ran, W. She, and J. Liu, “Modifying cement hydration with NS @ PCE core-shell nanoparticles,” *Advances in Materials Science and Engineering*, vol. 2017, Article ID 3823621, 13 pages, 2017.
  - [12] H. Dong, S.-R. Du, X.-Y. Zheng et al., “Lanthanide nanoparticles: from design toward bioimaging and therapy,” *Chemical Reviews*, vol. 115, no. 19, pp. 10725–10815, 2015.
  - [13] Y. Tang, H. Xin, F. Yang, and X. Long, “A historical review and bibliometric analysis of nanoparticles toxicity on algae,” *Journal of Nanoparticle Research*, vol. 20, no. 4, p. 92, 2018.
  - [14] A. M. Gazizulina, E. M. Alakshin, E. I. Baibekov et al., “Electron paramagnetic resonance of  $\text{Gd}^{3+}$  ions in powders of  $\text{LaF}_3:\text{Gd}^{3+}$  nanocrystals,” *JETP Letters*, vol. 99, no. 3, pp. 149–152, 2014.
  - [15] E. M. Alakshin, A. V. Klochkov, S. L. Korableva et al., “Magnetic properties of powders  $\text{LiTbF}_4$  and  $\text{TbF}_3$ ,” *Magnetic Resonance in Solids Electronic Journal*, vol. 18, no. 2, 2016.
  - [16] P. P. Fedorov, A. A. Luginina, S. V. Kuznetsov, and V. V. Osiko, “Nanofluorides,” *Journal of Fluorine Chemistry*, vol. 132, no. 12, pp. 1012–1039, 2011.
  - [17] M. S. Pudovkin, S. L. Korableva, A. O. Krashenninnicova et al., “Toxicity of laser irradiated photoactive fluoride  $\text{PrF}_3$  nanoparticles toward bacteria,” *Journal of Physics: Conference Series*, vol. 560, no. 1, article 012011, 2014.
  - [18] M. S. Pudovkin, D. A. Koryakovtseva, E. V. Lukinova et al., “Characterization of Pr-doped  $\text{LaF}_3$  nanoparticles synthesized by different variations of coprecipitation method,” *Journal of Nanomaterials*, vol. 2019, Article ID 7549325, 17 pages, 2019.
  - [19] W. Zhu, D. Chen, L. Lei, J. Xu, and Y. Wang, “An active-core/active-shell structure with enhanced quantum-cutting luminescence in Pr-Yb co-doped monodisperse nanoparticles,” *Nanoscale*, vol. 6, no. 18, pp. 10500–10504, 2014.
  - [20] V. V. Semashko, M. S. Pudovkin, A. C. Cefalas et al., “Tiny rare-earth fluoride nanoparticles activate tumour cell growth via electrical polar interactions,” *Nanoscale Research Letters*, vol. 13, no. 1, p. 370, 2018.
  - [21] M. S. Pudovkin, P. V. Zelenikhin, A. O. Krashenninnikova et al., “Photoinduced toxicity of  $\text{PrF}_3$  and  $\text{LaF}_3$  nanoparticles,” *Optics and Spectroscopy*, vol. 121, no. 4, pp. 538–543, 2016.
  - [22] M. S. Pudovkin, O. A. Morozov, V. V. Pavlov et al., “Physical background for luminescence thermometry sensors based on  $\text{Pr}^{3+}:\text{LaF}_3$  crystalline particles,” *Journal of Nanomaterials*, vol. 2017, Article ID 3108586, 9 pages, 2017.
  - [23] A. M. Korableva, M. K. Kaczmarek, and R. Van Deun, “ $\text{Er}^{3+}$ -to- $\text{Yb}^{3+}$  and  $\text{Pr}^{3+}$ -to- $\text{Yb}^{3+}$  energy transfer for highly efficient near-infrared cryogenic optical temperature sensing,” *Nanoscale*, vol. 11, no. 3, pp. 833–837, 2019.
  - [24] S. Sekiyama, M. Umezawa, S. Kuraoka, T. Ube, M. Kamimura, and K. Soga, “Temperature sensing of deep abdominal region in mice by using over-1000 nm near-infrared luminescence of rare-earth-doped  $\text{NaYF}_4$  nanothermometer,” *Scientific Reports*, vol. 8, no. 1, 2018.
  - [25] S. G. Pandya, J. P. Corbett, W. M. Jadwisieniczak, and M. E. Kordesch, “Structural characterization and X-ray analysis by Williamson-Hall method for erbium doped aluminum nitride nanoparticles, synthesized using inert gas condensation technique,” *Physica E: Low-Dimensional Systems and Nanostructures*, vol. 79, pp. 98–102, 2016.
  - [26] R. G. Chaudhuri and S. Paria, “Core/shell nanoparticles: classes, properties, synthesis mechanisms, characterization, and applications,” *Chemical Reviews*, vol. 112, no. 4, pp. 2373–2433, 2011.
  - [27] O. Hudak and M. Hudak, “Magnetic nanoparticles with core shell: macroscopic model and coercive field,” *Advances in Materials Science and Engineering*, vol. 2010, Article ID 909810, 6 pages, 2010.
  - [28] S. V. Kuznetsov, O. A. Morozov, V. G. Gorieva et al., “Synthesis and luminescence studies of  $\text{CaF}_2:\text{Yb}:\text{Pr}$  solid solutions powders for photonics,” *Journal of Fluorine Chemistry*, vol. 211, pp. 70–75, 2018.
  - [29] C. Li, X. Liu, P. Yang, C. Zhang, H. Lian, and J. Lin, “ $\text{LaF}_3$ ,  $\text{CeF}_3$ ,  $\text{CeF}_3:\text{Tb}^{3+}$ , and  $\text{CeF}_3:\text{Tb}^{3+}@\text{LaF}_3$  (core-shell) nanoparticles: hydrothermal synthesis and luminescence properties,” *The Journal of Physical Chemistry C*, vol. 112, no. 8, pp. 2904–2910, 2008.
  - [30] Y. Y. Bu, S. J. Cheng, X. F. Wang, and X. H. Yan, “Optical thermometry based on luminescence behavior of  $\text{Dy}^{3+}$ -doped transparent  $\text{LaF}_3$  glass ceramics,” *Applied Physics A*, vol. 121, no. 3, pp. 1171–1178, 2015.
  - [31] U. Rocha, K. Upendra Kumar, C. Jacinto et al., “ $\text{Nd}^{3+}$  doped  $\text{LaF}_3$  nanoparticles as self-monitored photo-thermal agents,” *Applied Physics Letters*, vol. 104, no. 5, article 053703, 2014.
  - [32] V. K. Rai, D. K. Rai, and S. B. Rai, “ $\text{Pr}^{3+}$  doped lithium tellurite glass as a temperature sensor,” *Sensors and Actuators A: Physical*, vol. 128, no. 1, pp. 14–17, 2006.
  - [33] M. Kaczkan, Z. Boruc, B. Fetlinski, S. Turczynski, and M. Malinowski, “Temperature dependence of  $^3\text{P}_0$   $\text{Pr}^{3+}$  fluorescence dynamics in  $\text{Y}_4\text{Al}_2\text{O}_9$  crystals,” *Applied Physics B*, vol. 113, no. 2, pp. 277–283, 2013.
  - [34] C. D. Brites, K. Fiaczyk, J. F. Ramalho, M. Sójka, L. D. Carlos, and E. Zych, “Widening the temperature range of luminescent thermometers through the intra- and interconfigurational transitions of  $\text{Pr}^{3+}$ ,” *Advanced Optical Materials*, vol. 6, no. 10, article 1701318, 2018.
  - [35] M. S. Pudovkin, P. V. Zelenikhin, V. Shtyryeva et al., “Coprecipitation method of synthesis, characterization, and cytotoxicity of  $\text{Pr}^{3+}:\text{LaF}_3$  ( $C_{\text{Pr}} = 3, 7, 12, 20, 30\%$ ) nanoparticles,” *Journal of Nanotechnology*, vol. 2018, Article ID 8516498, 9 pages, 2018.
  - [36] A. Vanetsev, K. Kaldvee, L. Puust et al., “Relation of crystallinity and fluorescent properties of  $\text{LaF}_3:\text{Nd}^{3+}$  nanoparticles synthesized with different water-based techniques,” *ChemistrySelect*, vol. 2, no. 17, pp. 4874–4881, 2017.
  - [37] S. G. Fedorenko, A. V. Popov, E. A. Vagapova, A. E. Baranchikov, and Y. V. Orlovskii, “Concentration self-quenching of luminescence in crystal matrices activated by  $\text{Nd}^{3+}$  ions: theory and experiment,” *Journal of Luminescence*, vol. 198, pp. 138–145, 2018.
  - [38] Y. V. Orlovskii, A. S. Vanetsev, K. Keevend et al., “NIR fluorescence quenching by OH acceptors in the  $\text{Nd}^{3+}$  doped  $\text{KY}_3\text{F}_{10}$  nanoparticles synthesized by microwave-hydrothermal treatment,” *Journal of Alloys and Compounds*, vol. 661, pp. 312–321, 2016.
  - [39] S. Sivakumar, P. R. Diamente, and F. C. J. M. van Veggel, “Silica-coated  $\text{Ln}^{3+}$ -doped  $\text{LaF}_3$  nanoparticles as robust down- and upconverting biolabels,” *Chemistry—A European Journal*, vol. 12, no. 22, pp. 5878–5884, 2006.

- [40] P. Scherrer, "Bestimmung der Grösse und der inneren Struktur von Kolloidteilchen mittels Röntgenstrahlen," *Nachrichten von der Gesellschaft der Wissenschaften zu Göttingen*, vol. 26, pp. 98–100, 1918.
- [41] R. Sivakami, S. Dhanuskodi, and R. Karvembu, "Estimation of lattice strain in nanocrystalline RuO<sub>2</sub> by Williamson-Hall and size-strain plot methods," *Spectrochimica Acta Part A: Molecular and Biomolecular Spectroscopy*, vol. 152, pp. 43–50, 2016.
- [42] J. Hegarty, D. L. Huber, and W. M. Yen, "Fluorescence quenching by cross relaxation in LaF<sub>3</sub>:Pr<sup>3+</sup>," *Physical Review B*, vol. 25, no. 9, pp. 5638–5645, 1982.
- [43] H. Okamoto, K. Kasuga, I. Hara, and Y. Kubota, "Visible-NIR tunable Pr<sup>3+</sup>-doped fiber laser pumped by a GaN laser diode," *Optics Express*, vol. 17, no. 22, pp. 20227–20232, 2009.
- [44] I. Kamma, P. Kommidi, and B. R. Reddy, "High temperature measurement using luminescence of Pr<sup>3+</sup> doped YAG and Ho<sup>3+</sup> doped CaF<sub>2</sub>," *Physica Status Solidi C*, vol. 6, no. S1, pp. S187–S190, 2009.
- [45] H. H. Caspers, H. E. Rast, and R. A. Buchanan, "Energy levels of Pr<sup>3+</sup> in LaF<sub>3</sub>," *The Journal of Chemical Physics*, vol. 43, no. 6, pp. 2124–2128, 1965.
- [46] D. Li, Y. Wang, X. Zhang, K. Yang, L. Liu, and Y. Song, "Optical temperature sensor through infrared excited blue upconversion emission in Tm<sup>3+</sup>/Yb<sup>3+</sup> codoped Y<sub>2</sub>O<sub>3</sub>," *Optics Communications*, vol. 285, no. 7, pp. 1925–1928, 2012.
- [47] M. Quintanilla, E. Cantelar, F. Cusso, M. Villegas, and A. C. Caballero, "Temperature sensing with up-converting submicron-sized LiNbO<sub>3</sub>:Er<sup>3+</sup>/Yb<sup>3+</sup> particles," *Applied Physics Express*, vol. 4, no. 2, article 022601, 2011.
- [48] L. Eyring, K. A. Gschneidner, and G. H. Lander, *Handbook on the Physics and Chemistry of Rare Earths*, vol. 32, Elsevier, Amsterdam, Netherlands, 2002.
- [49] S. Gharouel, L. Labrador-Páez, P. Haro-González, K. Horchani-Naifer, and M. Férid, "Fluorescence intensity ratio and lifetime thermometry of praseodymium phosphates for temperature sensing," *Journal of Luminescence*, vol. 201, pp. 372–383, 2018.
- [50] R. H. Page, K. I. Schaffers, L. D. DeLoach et al., "Cr<sup>2+</sup>-doped zinc chalcogenides as efficient, widely tunable mid-infrared lasers," *IEEE Journal of Quantum Electronics*, vol. 33, no. 4, pp. 609–619, 1997.
- [51] M. J. Weber, "Spontaneous emission probabilities and quantum efficiencies for excited states of Pr<sup>3+</sup> in LaF<sub>3</sub>," *The Journal of Chemical Physics*, vol. 48, no. 10, pp. 4774–4780, 1968.
- [52] M. Ren, C. D. S. Brites, S.-S. Bao, R. A. S. Ferreira, L.-M. Zheng, and L. D. Carlos, "A cryogenic luminescent ratiometric thermometer based on a lanthanide phosphonate dimer," *Journal of Materials Chemistry C*, vol. 3, no. 33, pp. 8480–8484, 2015.
- [53] E. Lukinova, E. Madirov, M. Pudovkin et al., "Luminescence decay of Sm: LaF<sub>3</sub>@LaF<sub>3</sub> core-shell crystalline nanoparticles," *EPJ Web of Conferences*, vol. 161, article 03012, 2017.
- [54] A. A. Ansari, J. P. Labis, and M. A. Manthrammel, "Synthesis, structural, and photoluminescence studies of LaF<sub>3</sub>:Pr, LaF<sub>3</sub>:Pr@LaF<sub>3</sub>, and LaF<sub>3</sub>:Pr@LaF<sub>3</sub>@SiO<sub>2</sub> nanophosphors," *Journal of the Australian Ceramic Society*, vol. 54, no. 3, pp. 493–500, 2018.
- [55] H. Wu, M. Fang, G. T. Fei, Z. M. Hu, and L. De Zhang, "LaF<sub>3</sub>:Pr<sup>3+</sup> hollow hexagon nanostructures via green and eco-friendly synthesis and their photoluminescence properties," *Journal of Materials Science*, vol. 54, no. 4, pp. 2897–2907, 2019.

